Engineering Temperature-Dependent Carrier Concentration in Bulk Composite Materials via Temperature-Dependent Fermi Level Offset

Si Hui, Wenpei Gao, Xu Lu, Anurag Panda, Trevor P. Bailey, Alexander A. Page, Stephen R. Forrest, Donald T. Morelli, Xiaoqing Pan, Kevin P. Pipe, and Ctirad Uher**

Precise control of carrier concentration in both bulk and thin-film materials is crucial for many solid-state devices, including photovoltaic cells, superconductors, and high mobility transistors. For applications that span a wide temperature range (thermoelectric power generation being a prime example) the optimal carrier concentration varies as a function of temperature. This work presents a modified modulation doping method to engineer the temperature dependence of the carrier concentration by incorporating a nanosize secondary phase that controls the temperature-dependent doping in the bulk matrix. This study demonstrates this technique by de-doping the heavily defect-doped degenerate semiconductor GeTe, thereby enhancing its average power factor by 100% at low temperatures, with no deterioration at high temperatures. This can be a general method to improve the average thermoelectric performance of many other materials.

1. Introduction

The performance metrics of many electronic device technologies depend on a carefully controlled charge carrier concentration.[1–11] However, the concentration that is optimal may be a strong function of temperature.[12] For example, the carrier concentration that maximizes the dimensionless thermoelectric (TE) figure of merit ZT (and thus the energy conversion efficiency) of a TE material depends upon the temperature, as illustrated in **Figure 1**a,b (which derives from expressions detailed in Section S1 of the Supporting Information). ZT is defined as $S^2\sigma T/\kappa$, where S is the Seebeck coefficient, σ is the electrical conductivity, T is the absolute temperature, and κ is the thermal conductivity. The temperature dependence of the optimal carrier concentration poses a challenge since TE devices are typically operated over a wide range of temperatures and, with a fixed carrier concentration, the performance degrades at temperatures for which the carrier concentration is not optimal. This problem is magnified by the fact that the figure of merit is also strongly temperature-dependent and is typically optimized by adjusting the carrier concentration near its peak value. Conventional doping strategies based on adding impurity atoms do not offer a means of controlling the temperature dependence of the carrier concentration because

Dr. S. Hui
Department of Mechanical Engineering
Department of Physics
University of Michigan
Ann Arbor, MI 48109, USA

Dr. W. Gao
Department of Chemical Engineering and Materials Science
University of California
Irvine, CA 92697, USA

Dr. X. Lu
Department of Chemical Engineering and Materials Science
Michigan State University
East Lansing, MI 48824, USA

A. Panda
Department of Materials Science and Engineering
University of Michigan
Ann Arbor, MI 48109, USA

T. P. Bailey, Dr. A. A. Page, Prof. C. Uher
Department of Physics
University of Michigan
Ann Arbor, MI 48109, USA
E-mail: cuher@umich.edu

Prof. S. R. Forrest
Department of Physics
Department of Materials Science and Engineering
Department of Electrical Engineering and Computer Science
University of Michigan
Ann Arbor, MI 48109, USA

Prof. D. T. Morelli
Department of Chemical Engineering and Materials Science
Department of Physics and Astronomy
Michigan State University
East Lansing, MI 48824, USA

Prof. X. Pan
Department of Chemical Engineering and Materials Science
Department of Physics and Astronomy
University of California
Irvine, CA 92697, USA

Prof. K. P. Pipe
Department of Mechanical Engineering
Department of Electrical Engineering and Computer Science
University of Michigan
Ann Arbor, MI 48109, USA
E-mail: pipe@umich.edu

DOI: 10.1002/aenm.201701623

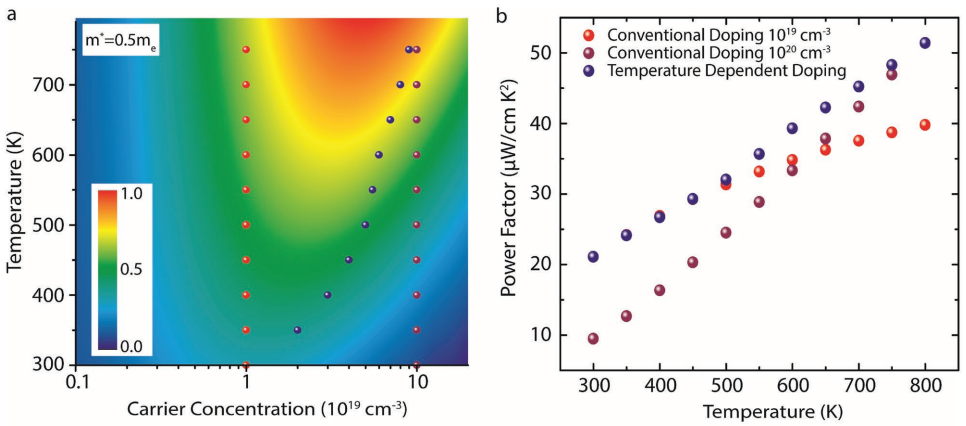

Figure 1. a) Normalized power factor as a function of carrier concentration and temperature for a single parabolic band with effective mass of 0.5 m_e. Blue spheres represent a temperature-dependent carrier concentration. The red and purple spheres represent temperature-independent carrier concentrations optimizing the power factor at low temperature and high temperature, respectively. b) Temperature-dependent power factor corresponding to the three sets of spheres shown in (a). Numerical results indicate that a varying carrier concentration is desired to enhance the average power factor over a wide temperature range. The conventional impurity doping method can only optimize the power factor at one particular temperature.

the dopant ionization energy is usually quite low such that essentially all are ionized at relatively low temperatures.[13,14] Moreover, limited solubility and low doping efficiency of elements in a given matrix may also limit the carrier concentration range that can be achieved.[15]

Various approaches have been proposed to enhance the temperature-averaged performance of thermoelectric materials. A high average ZT over a wide range of temperature has recently been realized in K-doped $PbTe_{0.7}S_{0.3}$ composites that have a low thermal conductivity as well as a band-gap opening at elevated temperatures.[16] Another example is heavily doped p-type single crystals of SnSe that benefit from an increased number of band pockets near the Fermi level.[17] Attempts to achieve temperature-dependent doping have also been made, such as exploring the temperature-dependent solubility of Ag in a PbTe matrix[12] and studying temperature-dependent dopant migration in multiphase $(PbTe)_{0.65}(PbS)_{0.25}(PbSe)_{0.1}$ composites.[18] However, all these examples critically depend on a specific material property (e.g., temperature-dependent bandgap opening, multicarrier pocket band structure, and temperature-dependent solubility) thus severely constraining their application to a wide range of materials. While highly desirable, a more general temperature-dependent doping method has, to our knowledge, not yet been proposed.

A useful alternative to impurity doping is modulation doping,[19] first demonstrated in GaAs–$Al_xGa_{1-x}As$ heterojunction superlattices by Dingle et al. By intentionally separating doped regions from transport pathways, charge carrier mobilities in modulated structures can attain exceptionally high values. Modulation doping has been used in 2D electron gases to achieve a very high mobility by inserting a single-unit-cell insulating layer,[20] in photoinduced modulation doped graphene/boron nitride heterojunctions,[21] in quasi-1D Ge–Si_xGe_{1-x} core-shell nanowire electron systems with enhanced mobility,[22] and in p-type CdS nanowires with high hole mobility for photovoltaic applications.[23] In addition to low dimensional structures and devices, modulation doping has recently been demonstrated as an effective method for enhancing carrier mobility in 3D bulk materials, especially those intended for thermoelectric applications.[24–27] In spite of these successes, to the best of our knowledge no temperature-dependent doping scheme based on modulation doping has been demonstrated.

Inspired by modulation doping, which utilizes the Fermi level offset between two neighboring regions to provide charge carrier transfer, we examine the prospect of temperature tuning such offsets to realize a temperature-dependent carrier concentration. This is achieved by creating nanoscale inclusions of a secondary phase that has a temperature dependence of its Fermi level which is significantly different than that of the bulk, offering a means for temperature-tuning the bulk carrier concentration. In this work, we demonstrate the technique in a GeTe–$CuInTe_2$ composite structure. Since incorporating a secondary phase in the matrix is not restricted by a solubility limit or doping efficiency, the choice of the compounds (secondary phase materials) is much larger than that of conventional dopants, and thus this method potentially encompasses a large pool of candidate materials.

Details concerning composite materials synthesis, structural characterization, and transport property measurements are given in Section 4. We note that the composite structures are of the form $(Ge_2Te_2)_x(CuInTe_2)_{1-x}$, where x = 100, 98, 95, 90, 87.5, 85, 70, 30, and 10 (expressed as a percentage). The structures are designated as GT-x. For example, GT-90 stands for $(Ge_2Te_2)_{0.9}(CuInTe_2)_{0.1}$.

2. Results and Discussion

While numerous material properties can contribute to a temperature-dependent carrier concentration (e.g., a phase transition or temperature-dependent band structure), charge transfer at an interface is strongly influenced by a Fermi level offset that can be highly temperature-dependent. The resulting band bending and charge transfer, including their dependence on the Fermi level offset, can be quantitatively described by self-consistent solutions of the drift-diffusion and Poisson equations.

To assess the impact of Fermi level offset temperature dependence on charge transfer temperature dependence, we

numerically solved a 3D spherically symmetric interface charge transfer problem using a fourth-order Runge–Kutta algorithm with the shooting method.[28] Details of the model are given in Section S2 of the Supporting Information.

The band bending and charge distribution profiles, as well as the average carrier concentration change in the matrix, depend on many parameters, including the Fermi level offset, band structure of each phase, dielectric constant of each phase, electrostatic potential drop across the interface, original carrier concentration in each phase, size of the secondary phase inclusions, and secondary phase volume fraction, all of which have been taken into account. Other parameters not included in the model, such as surface states, charge accumulation, and non-spherical inclusion shape may also influence the results. Here we focus on the parameters that may significantly change with temperature or be controlled in the GeTe–$CuInTe_2$ system, such as the Fermi level offset, secondary inclusion size, secondary phase volume fraction, and inclusion shape. The average bulk matrix carrier concentration change, which depends on the shape, size, and molar concentration of the secondary phase (which we refer to as "doping ratio"), is shown in **Figure 2**a,b. It is worth noting that forming nanosize (rather than micro-size) secondary phases is crucial to altering the carrier concentration in heavily doped materials, since the depletion width decreases as the carrier concentration increases. Moreover, the surface-to-volume ratio of the secondary phase inclusions can have a significant influence.

As an example of how charge transfer at interfaces can induce a temperature-dependent carrier concentration, we consider a typical heterojunction in Figure 2c. The secondary phase material has a much weaker Fermi level temperature dependence due to a temperature-independent band structure, and the matrix material exhibits temperature-dependent band convergence, such as found in group IV–VI compounds.[14,29] As temperature increases, the Fermi level offset decreases. The convergence of the Fermi levels significantly alters the charge transfer across the interface and thus the average bulk matrix carrier concentration, as shown in Figure 2c,d.

The GeTe matrix is a degenerately self-doped semiconductor with a rhombohedral structure at room temperature and a carrier concentration of approximately 8×10^{20} cm^{-3}.[30] It is characterized by a relatively high TE power factor at high

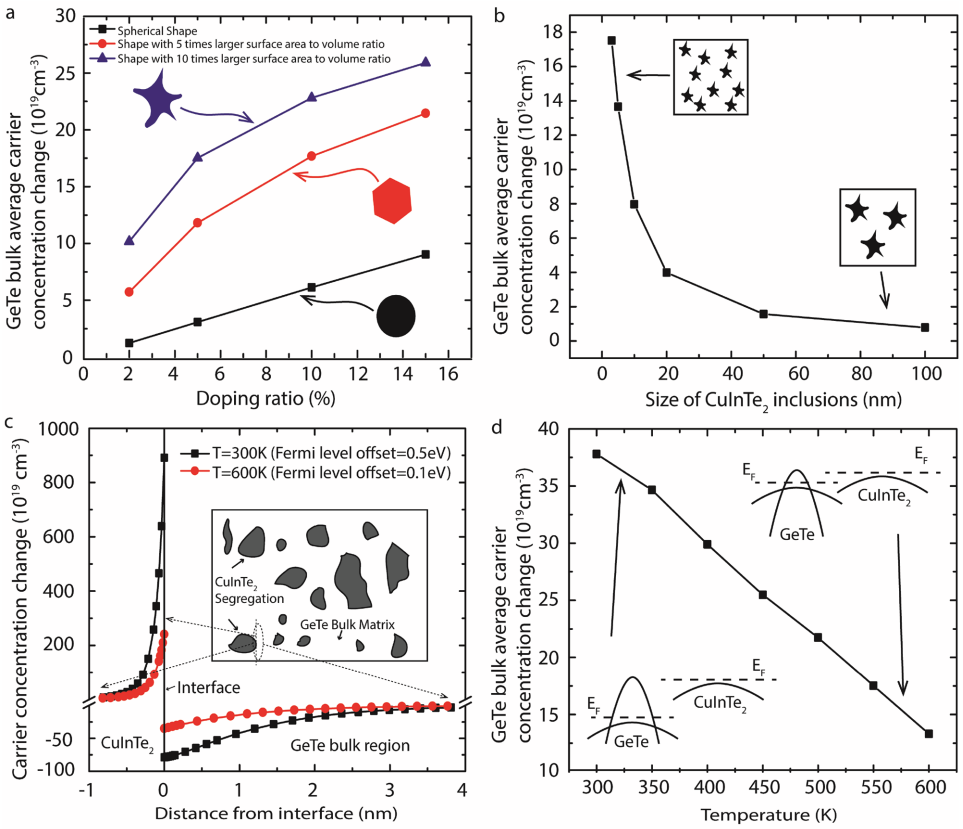

Figure 2. a) Average room temperature carrier concentration depletion in the bulk region as a function of secondary phase concentration ("doping ratio") with various surface-to-volume ratios assumed for the secondary phase inclusions. The size of the secondary phase is set to be 3 nm. b) Average room temperature carrier concentration depletion over the bulk region as a function of the size of $CuInTe_2$ inclusions. The doping ratio is set to be 5 mol% and the surface-to-volume ratio is set to be 10 times of that of a sphere. Inclusion size is defined by the mean curvature of the shape. c) Calculated carrier concentration change profile at 300 and 600 K near the interface between GeTe and $CuInTe_2$ phases. The Fermi level offset between the matrix and secondary phase is set to be 0.5 eV at room temperature and 0.1 eV at 600 K, corresponding to the Fermi level convergence in the GeTe–$CuInTe_2$ system. Inset: 2D illustration of the distribution of secondary phase inclusions. d) Average carrier concentration depletion over the bulk region as a function of temperature assuming the Fermi level offset is a linear function of temperature. A secondary phase surface-to-volume ratio 10 times of that of a sphere and $CuInTe_2$ doping ratio of 5 mol% are assumed.

temperatures due to the convergence of two valence bands, but also a relatively poor performance at lower temperatures due to its high carrier concentration.[29,31] On the other hand, $CuInTe_2$ is a ternary chalcopyrite with a tetragonal structure and a low carrier concentration of approximately 10^{18} cm^{-3} that has drawn attention for thermoelectric applications due to its low thermal conductivity.[32] Density functional theory (DFT) calculations were performed to obtain the band structure of $CuInTe_2$ at $T = 0$.[33,34] Based on the calculated band structure, high-temperature transport properties were calculated by solving the Boltzmann transport equation and assuming a temperature-independent band structure. The calculated transport properties agree with the experimental results, supporting the assumption of a temperature-independent band structure for $CuInTe_2$.[33,34] We selected this compound as the secondary phase de-dopant because it has a more rigid band structure than GeTe as temperature is changed.

The dissimilar crystal structures of GeTe and $CuInTe_2$ result in both micro and nanoscale segregation of $CuInTe_2$, as corroborated by energy dispersive X-ray spectroscopy (EDS) mapping and transmission electron microscopy (TEM) data shown in **Figure 3**a,b. Details regarding density, X-ray diffraction (XRD), and scanning electron microscopy (SEM) data are provided in Section S3 of the Supporting Information. It is worth noting that XRD, EDS mapping, and SEM all indicate that only GeTe and $CuInTe_2$ form as the major phases. EDS mapping and SEM also confirm that the distribution of micrometer-size inclusions is homogeneous. Observations of nanoscale $CuInTe_2$ inclusions in multiple randomly selected regions confirm the existence, size, and shape of the $CuInTe_2$ secondary phases, as shown in Figure 3b–d.

We also performed EDS 2D mapping and a line scan to confirm the nanoscale size and distribution of the $CuInTe_2$ inclusions in the matrix, as shown in Figure 3e. The room temperature Fermi level offset between GeTe and $CuInTe_2$ bulk is 0.3 ± 0.2 eV as determined from the onset of the ultraviolet photoemission spectroscopy (UPS) peak in the low kinetic energy range, **Figure 4**a. The onset energy for the composite with 5% $CuInTe_2$ shifts by 0.2 eV from GeTe to $CuInTe_2$, suggesting band bending caused by a high interface density (which we define as the total interfacial area per unit volume).[35] This shift is also observed in the X-ray photoemission spectroscopy (XPS) core levels, as shown as Figure 4b.

The transport properties of the GeTe–$CuInTe_2$ composites from room temperature to 800 K are consistent with the carrier concentration depletion model, as shown in **Figure 5**a–c.

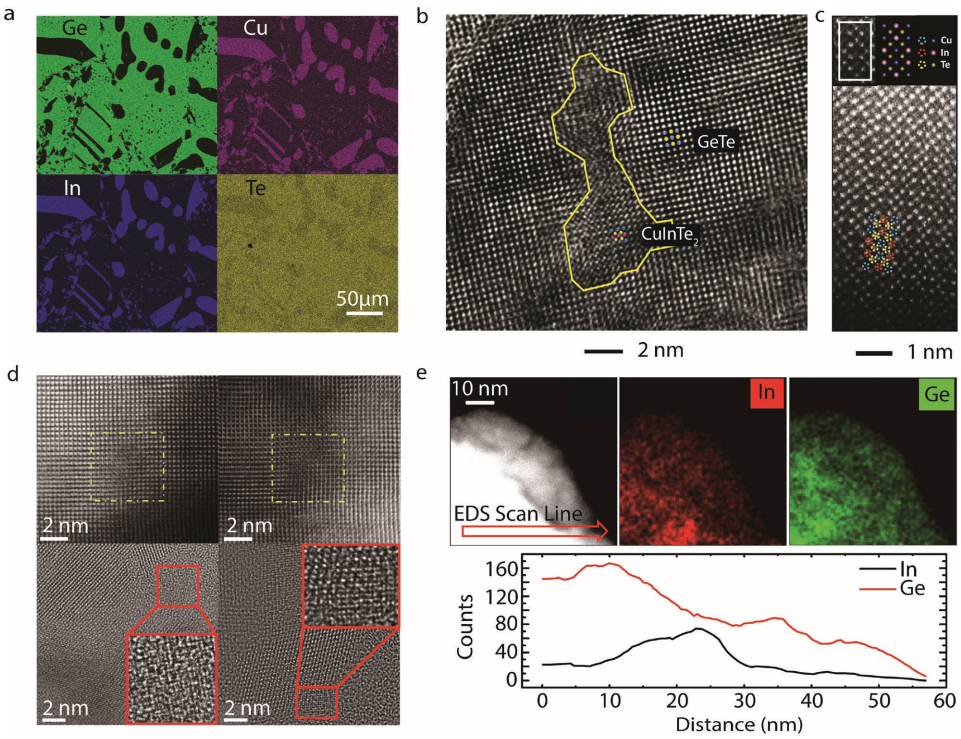

Figure 3. a) EDS mapping of Ge, Cu, In, and Te elements in the GT-70 sample, which is 30% $CuInTe_2$. Light regions represent the presence of the corresponding element. b) High resolution TEM image of a small region of the GT-70 sample. The GeTe matrix has a rhombohedral structure that matches the overlaid GeTe atomic model. The area circled with a yellow line shows an atomic lattice corresponding to the chalcopyrite $CuInTe_2$ structure, confirming the existence of the nanosize $CuInTe_2$ secondary phase. The shape of these nanosize segregations is not spherical. c) High angle annular dark field (HAADF) scanning transmission electron microscopy (STEM) *z*-contrast image of a $CuInTe_2$ region. Atomic columns of Cu, In, and Te are identified by the intensity corresponding to the atomic number of each element. d) The top two images are *z*-contrast and bright field STEM image of the GT-95 sample. The $CuInTe_2$ inclusion is highlighted in the yellow box. The bottom two images are high resolution TEM images of GT-95. Small areas of $CuInTe_2$ are highlighted and zoomed-in in the red boxes. e) EDS mapping of the Ge and In in GT-95. The HAADF image is in grayscale, the Ge map is in green, and the In map is in red. The red arrow indicates the EDS line scan position and direction. The local In and Ge variations reflect the distribution of nanoscale $CuInTe_2$ inclusions.

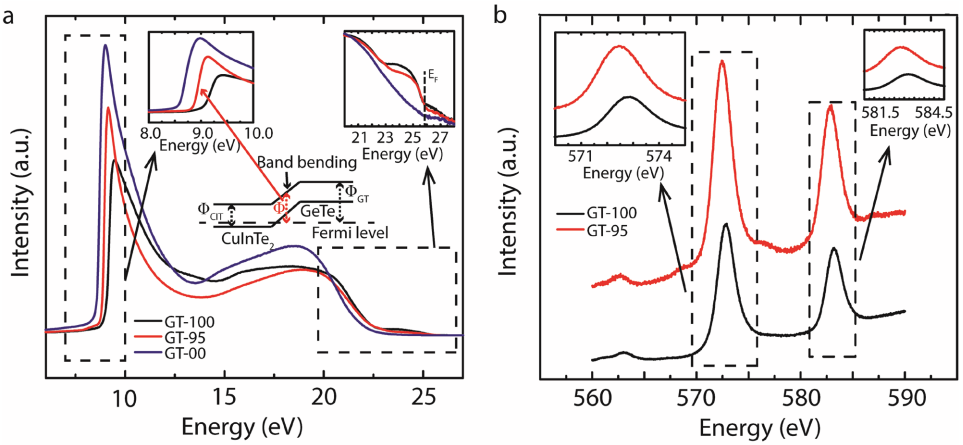

Figure 4. a) UPS results for the GT-100, GT-95, and GT-00 samples. The work function shift observed in the GT-95 sample suggests a high interface density since the Fermi level is spatially constant and the local vacuum level bends with band bending, as illustrated in the middle inset. The top insets are zoomed-in data for the lower (left) and higher (right) kinetic energy ranges. The right inset verifies that the Fermi levels of the three tested samples are all aligned with the measurement system during the measurement, calibrated by measuring the Fermi step of a freshly deposited Au film. b) XPS Te-3d core levels. The insets show the energy shift of the two peaks.

The transport properties of pure GeTe are similar to those measured previously.[29] Temperature-dependent Fermi levels in pure GeTe and $CuInTe_2$ were derived from their temperature-dependent transport coefficients as shown in the inset of Figure 5a, with details found in Section S1 of the Supporting Information. The temperature dependence of the Fermi level is stronger in GeTe than in $CuInTe_2$ due to the convergence of the GeTe light valence *L* band and heavy Σ band. Indeed, the

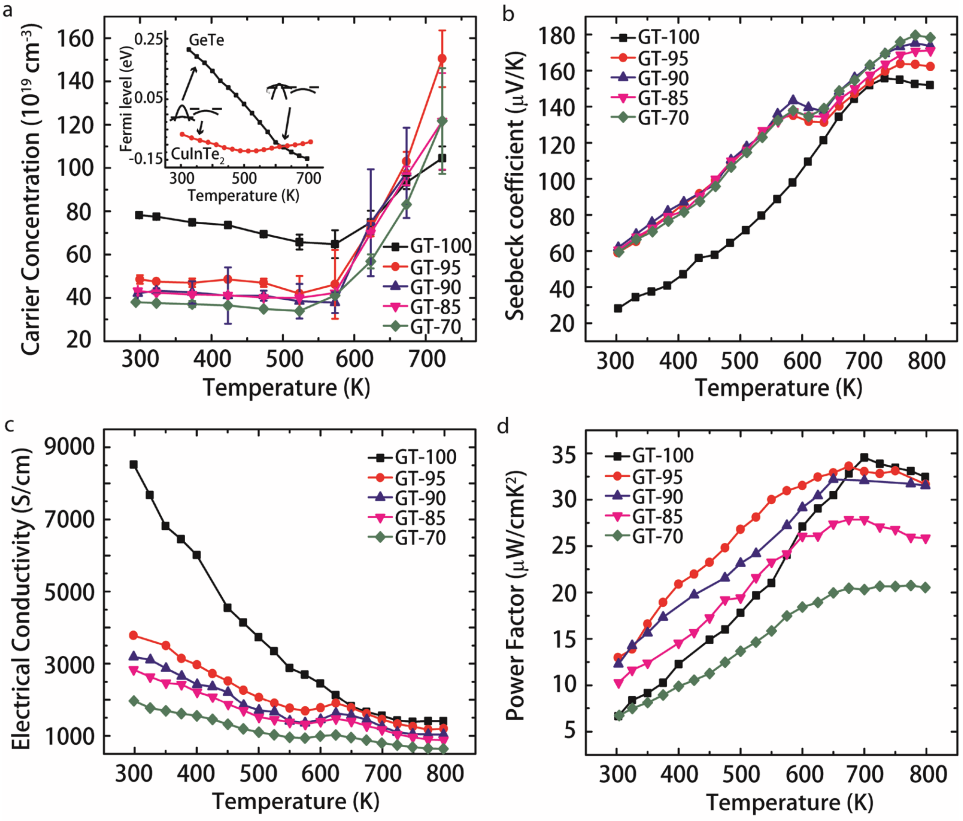

Figure 5. a–c) Temperature-dependent carrier concentration, Seebeck coefficient, and electrical conductivity for the GT-100, GT-95, GT-90, GT-85, and GT-70 samples. The inset in (a) shows the temperature-dependent Fermi levels of pure GeTe and $CuInTe_2$, derived from the measured transport coefficients. The room temperature offset was set to be 0.3eV based on the results of UPS. d) Temperature-dependent thermoelectric power factor of GT-100, GT-95, GT-90, GT-85, and GT-70 samples.

large Fermi level offset of approximately 0.3 eV at room temperature shrinks to nearly zero at 600 K, resulting in significantly weakened band bending near the interface, consistent with Figure 2c,d. The disappearance of the Fermi level offset between GeTe and $CuInTe_2$ phases at 600 K causes an anomalous decrease in the Seebeck coefficient, increase in the electrical conductivity, and increase in the carrier concentration. The Fermi level offset at temperatures below 600 K depletes carriers in the GeTe matrix, which results in reduced carrier concentration and electrical conductivity and an enhanced Seebeck coefficient. Carrier depletion at lower temperatures brings the carrier concentration in the GeTe matrix closer to the value that is optimal (i.e., maximizing the power factor) at each temperature in this lower range. As the Fermi level offset becomes small at higher temperatures, the dedoping effect ceases to influence the high temperature transport properties. As shown in Figure 5d, an enhanced average power factor is achieved in both the GT-95 and GT-90 samples, consistent with the prediction shown as the blue dots in Figure 1b.

It is necessary to exclude several other possible effects that could influence transport properties in the same manner as the modeled doping effects near room temperature: (1) Cu and In could fill defect sites in the GeTe matrix and thus reduce the carrier concentration; (2) energy filtering caused by the microscale and nanoscale $CuInTe_2$ inclusions could enhance the Seebeck coefficient while decreasing the electrical conductivity and carrier concentration; (3) strain caused by the $CuInTe_2$ inclusions could affect the transport properties of the GeTe matrix; and (4) interface states could reduce the carrier concentration in the GeTe matrix.

Regarding the first possible alternative effect, heat capacity measurements show a 15 K decrease in the phase transition temperature of all composites with respect to that of pure GeTe, as shown in **Figure 6**a. Together with the segregation of $CuInTe_2$ observed in backscattered electron (BSE) imaging of GT-98 (Figure S2a, Supporting Information), this confirms that the solubility of Cu and In in the GeTe matrix are below 2%. The room temperature mobility of the GeTe–$CuInTe_2$ composites is consistent with scattering by 1% impurities and nanoscale segregates (Section S4, Supporting Information) and is significantly larger than that of impurity-doped GeTe alloys such as GeTe–In_2Te_3 alloys.[31] The influence of 2% $CuInTe_2$ on the room temperature transport properties is less than that caused by 5% $CuInTe_2$, as shown in Figure 6c.

Regarding the second possible alternative effect, changes in the energy dependence of mobility can affect the Seebeck coefficient. Scattering from nanoscale inclusions has an $E^{3/2}$ energy dependence, whereas scattering by defects or acoustic phonons follows an $E^{-1/2}$ dependence.[14] For the composites in this study, modeling suggests that scattering by nanoscale

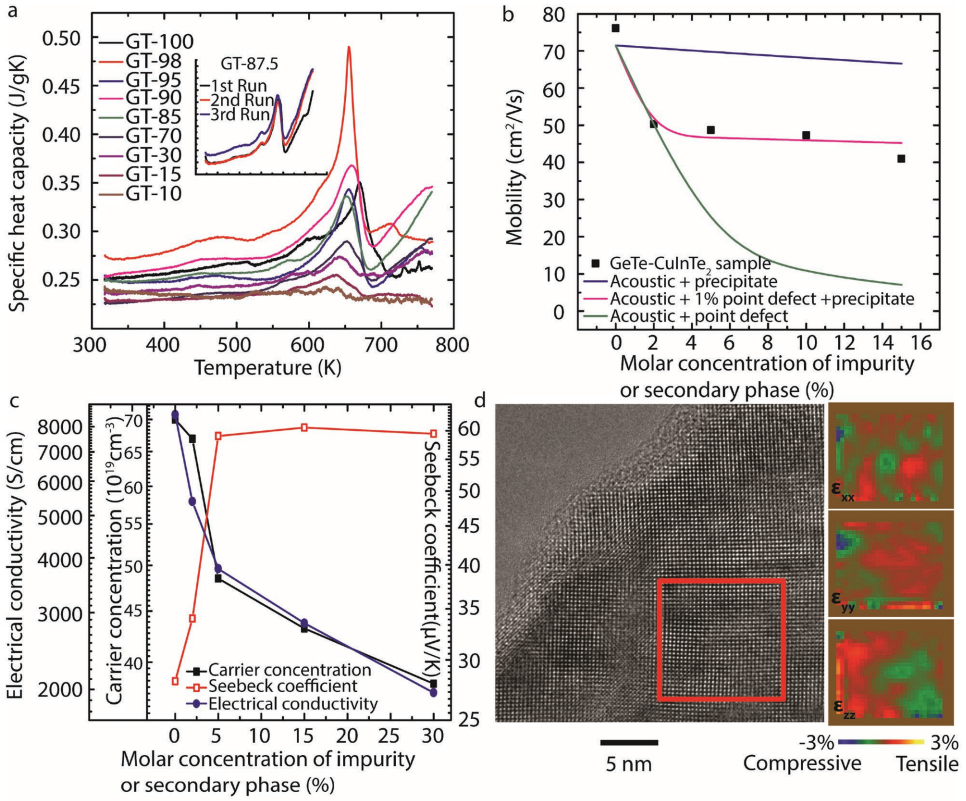

Figure 6. a) Temperature-dependent specific heat capacity of GT-*x* (with *x* = 100, 98, 95, 90, 85, 70, 30, 15, and 10) samples. Results of three consecutive measurements on the GT-87.5 sample are shown in the inset of (a). b) Room temperature mobilities as a function of the molar concentration of a modeled impurity or the secondary ($CuInTe_2$) phase. The mobility calculated for various scattering mechanisms is represented as solid lines. c) Room temperature carrier concentration, Seebeck coefficient, and electrical conductivity as a function of the molar concentration of the secondary phase. d) Strain mapping of the GeTe matrix at various distance away from the segregated secondary phase obtained from a high resolution TEM image.

inclusions contributes only a very small amount to the total charge carrier scattering (Figure 6b) and hence is expected to have little impact on the energy dependence of the mobility. For some materials, micrometer-scale inclusions may block low energy carriers and enhance the average energy of charge carriers, increasing the Seebeck coefficient, but for the composites in this study, the increasing number and size of $CuInTe_2$ micrograins reduces the electrical conductivity and does not enhance the Seebeck coefficient, as shown in Figure 6c. This suggests that $CuInTe_2$ inclusions block carriers of all energies, consistent with the room temperature band alignment. Thus, the observed room temperature transport properties do not appear to be influenced by energy filtering. Regarding strain effects, TEM analysis shows that the strain within the matrix fluctuates by only 1–2%, as shown in Figure 6d; such small fluctuations are unlikely to be responsible for the large changes in carrier concentration observed. Finally, estimates for carrier concentration reduction in the matrix caused by interface states (details provided in the Supporting Information) suggest that their contribution is insufficient to account for the observed reduction.

3. Conclusion

In summary, we demonstrate a general method whereby the carrier concentration can be adjusted within a large temperature range to enhance the temperature-averaged performance of a thermoelectric material. This temperature-dependent doping mechanism is based on incorporating nanosize secondary phases with appropriate Fermi level offset temperature dependences, which can be realized in a diverse class of materials. Various methods (e.g., phase transition, strain, magnetic field) may be used to control the temperature dependence of the Fermi level offset and hence the temperature dependence of the carrier concentration. The extension of this mechanism from bulk materials to thin film structures is straightforward and could support applications in the fields of photonics, electronics, and superconductors. Reduced scattering from nanosize precipitates compared to that from elemental impurities results in a higher mobility of charge carriers than conventional impurity doping.

4. Experimental Section

Synthesis: Raw elements of germanium, copper, indium, and tellurium were purchased from Alfa Aesar with the following purities: Ge (pieces, 99.9999+%), Cu (shot, 99.98%), In (ingots, 99.9999+%), and Te (lumps, 99.999+%). The starting materials were weighed according to the stoichiometric ratio $(Ge_2Te_2)_x(CuInTe_2)_{100-x}$ with x = 100, 98, 95, 90, 87.5, 85, 70, 30, and 10 in the glovebox under an argon atmosphere with oxygen and water levels below 0.1 and 0.5 ppm, respectively. In this paper, the samples were denoted as GT-x, where x represents the molar concentration of GeTe in the sample (expressed as a percentage). The weighed materials were then put in carefully cleaned quartz ampoules, sealed under a pressure of less than 10^{-4} Torr, and placed in a furnace heated according to the following schedule: slow heating up to 1000 °C at a rate of 1.5 °C min^{-1}; rest at 1000 °C for 12 h; slow cooling to 600 °C at 2 °C min^{-1}; annealing at 600 °C for 4 d; and slow cooling to room temperature at 2 °C min^{-1}. The as-cast ingots were hand-milled to powders under argon atmosphere and hot-pressed for 30 min. at a temperature of approximately 500 °C under a pressure of approximately 60 MPa.

Powder X-Ray Diffraction: GT-x samples were ground to fine powders and placed into aluminum holders for room temperature powder X-ray diffraction measurements using a Rigaku Ultima IV X-Ray diffractometer utilizing 2.2 kW Cu K-α radiation. The diffraction signal was collected from 5° to 90° at the rate of 2° min^{-1} with 0.05° steps. Measured peaks were compared with the peaks of the known compound (from a reference library) to identify the phases present.

Transport Property Measurements: 10 mm × 3 mm × 3 mm bars were cut from the hot pressed pellets for high temperature Seebeck coefficient and electrical conductivity measurements. Both the high temperature (from room temperature to 800 K) and low temperature (from 80 K to room temperature) transport properties were measured using custom setups. For high temperature Hall measurements, bar-shaped samples were cut with dimensions of 8 mm × 3 mm × 1 mm. High temperature Hall coefficients were measured using custom equipment with a superconducting magnet. For high temperature thermal conductivity studies, disk-shaped samples with 10 mm diameter and 1 mm thickness were used. Thermal conductivity was computed from the equation $\kappa = \lambda \times C_p \times \rho$, where κ, λ, C_p, and ρ represent the thermal conductivity, thermal diffusivity, specific heat capacity, and density, respectively. Measurements of thermal diffusivity were made using an Anter Flashline 3000 laser flash system, specific heat capacity was determined with the aid of a Pegasus 404 differential scanning calorimeter from Netzsch, and the densities of the pellets were determined by the Archimedes method.

Electron Microprobe Measurements: Composition mapping and surface topography of the samples were characterized with the help of EDS, BSE, and SEM implemented within a FEI Helios 650 Dualbeam Focused Ion Beam Workstation and Scanning Electron Microscope on carefully polished samples. TEM imaging was carried out on a Titan S/TEM at 300 kV at the Center for Nanophase Materials Sciences at Oak Ridge National Laboratory.

Ultraviolet and X-Ray Photoemission Spectroscopy: Photoemission spectroscopy measurements were carried out in an ultrahigh-vacuum chamber with pressure $<1 \times 10^{-9}$ Torr using 21.22 eV Helium-I (Ultraviolet) and 1486.7 eV Al Kα (X-ray) emissions. Samples were polished and stored under an Ar environment to prevent surface oxidation before being transferred into the system through a N_2-filled glovebox. Spectra were collected using a hemispherical electron energy analyzer (Thermo VG). To minimize sample charging, electrical contact was maintained via a metal clip attached to a copper puck connected to ground. Samples were biased at −9.00 V to ensure collection of low kinetic energy electrons.

Supporting Information

Supporting Information is available from the Wiley Online Library or from the author.

Acknowledgements

Financial support for this investigation was provided by the U. S. Department of Energy (DOE), U.S.-China Clean Energy Research Center (CERC-CVC) under Award No. DE-PI0000012. The hot-pressing process at Michigan State University was supported as part of the Center for Revolutionary Materials for Solid State Energy Conversion, an Energy Frontier Research Center funded by the U.S. Department of Energy, Office of Science, Office of Basic Energy Sciences, under Award No. DE-SC0001054. Financial support for UPS and XPS was provided by the U.S. Army Research Office (S.R.F. and A.P.). Financial support for BSE, SEM, and EDS was provided by the University of Michigan College of Engineering. W.G. was supported by the National Science Foundation with Grant No. CBET-1159240 and the School of Engineering at the

University of California, Irvine. TEM imaging and analysis were carried out at Irvine Materials Research Institute at the University of California, Irvine, and the Center for Nanophase Materials Sciences at Oak Ridge National Laboratory (ORNL). The authors would like to thank Dr. Miaofang Chi of ORNL for TEM imaging and analysis, and P. Gao and T. P. Hogan of Michigan State University for their confirmatory measurement of thermal diffusivity and heat capacity. S.H. also thanks H. Sun and H. Chi for helpful discussions.

Conflict of Interest

The authors declare no conflict of interest.

Keywords

composite materials, modulation doping, thermoelectric materials

Received: June 13, 2017
Revised: July 14, 2017
Published online: September 14, 2017

[1] J. M. Luther, P. K. Jain, T. Ewers, A. P. Alivisatos, *Nat. Mater.* **2011**, *10*, 361.
[2] A. Boltasseva, H. A. Atwater, *Science* **2011**, *331*, 290.
[3] X. Z. Lan, S. Masala, E. H. Sargent, *Nat. Mater.* **2014**, *13*, 233.
[4] M. Graetzel, R. A. J. Janssen, D. B. Mitzi, E. H. Sargent, *Nature* **2012**, *488*, 304.
[5] N. M. Gabor, J. C. W. Song, Q. Ma, N. L. Nair, T. Taychatanapat, K. Watanabe, T. Taniguchi, L. S. Levitov, P. Jarillo-Herrero, *Science* **2011**, *334*, 648.
[6] J. Wu, O. Pelleg, G. Logvenov, A. T. Bollinger, Y. J. Sun, G. S. Boebinger, M. Vanevic, Z. Radovic, I. Bozovic, *Nat. Mater.* **2013**, *12*, 877.
[7] A. Gozar, G. Logvenov, L. F. Kourkoutis, A. T. Bollinger, L. A. Giannuzzi, D. A. Muller, I. Bozovic, *Nature* **2008**, *455*, 782.
[8] M. H. Whangbo, C. C. Torardi, *Science* **1990**, *249*, 1143.
[9] C. Richter, H. Boschker, W. Dietsche, E. Fillis-Tsirakis, R. Jany, F. Loder, L. F. Kourkoutis, D. A. Muller, J. R. Kirtley, C. W. Schneider, J. Mannhart, *Nature* **2013**, *502*, 528.
[10] A. Ohtomo, H. Y. Hwang, *Nature* **2004**, *427*, 423.
[11] S. Thiel, G. Hammerl, A. Schmehl, C. W. Schneider, J. Mannhart, *Science* **2006**, *313*, 1942.
[12] Y. Z. Pei, A. F. May, G. J. Snyder, *Adv. Energy Mater.* **2011**, *1*, 291.
[13] R. Enderlein, N. J. M. Horing, *Fundamentals of Semiconductor Physics and Devices*, World Scientific, Singapore **1997**.
[14] Y. I. Ravich, B. A. Efimova, I. A. Smirnov, *Semiconducting Lead Chalcogenides*, Plenum, New York **1970**.
[15] S. Hui, M. D. Nielsen, M. R. Homer, D. L. Medlin, J. Tobola, J. R. Salvador, J. P. Heremans, K. P. Pipe, C. Uher, *J. Appl. Phys.* **2014**, *115*, 103704.
[16] H. J. Wu, L. D. Zhao, F. S. Zheng, D. Wu, Y. L. Pei, X. Tong, M. G. Kanatzidis, J. Q. He, *Nat. Commun.* **2014**, *5*, 4515.
[17] K. L. Peng, X. Lu, H. Zhan, S. Hui, X. D. Tang, G. W. Wang, J. Y. Dai, C. Uher, G. Y. Wang, X. Y. Zhou, *Energy Environ. Sci.* **2016**, *9*, 454.
[18] S. A. Yamini, D. R. G. Mitchell, Z. M. Gibbs, R. Santos, V. Patterson, S. Li, Y. Z. Pei, S. X. Dou, G. J. Snyder, *Adv. Energy Mater.* **2015**, *5*, 1501047.
[19] R. Dingle, H. L. Stormer, A. C. Gossard, W. Wiegmann, *Appl. Phys. Lett.* **1978**, *33*, 665.
[20] Y. Z. Chen, F. Trier, T. Wijnands, R. J. Green, N. Gauquelin, R. Egoavil, D. V. Christensen, G. Koster, M. Huijben, N. Bovet, S. Macke, F. He, R. Sutarto, N. H. Andersen, J. A. Sulpizio, M. Honig, G. E. D. K. Prawiroatmodjo, T. S. Jespersen, S. Linderoth, S. Ilani, J. Verbeeck, G. Van Tendeloo, G. Rijnders, G. A. Sawatzky, N. Pryds, *Nat. Mater.* **2015**, *14*, 801.
[21] L. Jun, J. Velasco, E. Huang, S. Kahn, C. Nosiglia, H. Z. Tsai, W. Yang, T. Taniguchi, K. Watanabe, Y. Zhang, G. Zhang, M. Crommie, A. Zettl, F. Wang, *Nat. Nanotechnol.* **2014**, *9*, 348.
[22] D. C. Dillen, K. Kim, E. S. Liu, E. Tutuc, *Nat. Nanotechnol.* **2014**, *9*, 116.
[23] F. Z. Li, L. B. Luo, Q. D. Yang, D. Wu, C. Xie, B. Nie, J. S. Jie, C. Y. Wu, L. Wang, S. H. Yu, *Adv. Energy Mater.* **2013**, *3*, 579.
[24] D. Wu, Y. L. Pei, Z. Wang, H. J. Wu, L. Huang, L. D. Zhao, J. Q. He, *Adv. Funct. Mater.* **2014**, *24*, 7763.
[25] Y. L. Pei, H. J. Wu, D. Wu, F. S. Zheng, J. Q. He, *J. Am. Chem. Soc.* **2014**, *136*, 13902.
[26] B. Yu, M. Zebarjadi, H. Wang, K. Lukas, H. Z. Wang, D. Z. Wang, C. Opeil, M. Dresselhaus, G. Chen, Z. F. Ren, *Nano. Lett.* **2012**, *12*, 2077.
[27] M. Zebarjadi, G. Joshi, G. H. Zhu, B. Yu, A. Minnich, Y. C. Lan, X. W. Wang, M. Dresselhaus, Z. F. Ren, G. Chen, *Nano. Lett.* **2011**, *11*, 2225.
[28] S. V. Faleev, F. Leonard, *Phys. Rev. B* **2008**, *77*, 214304.
[29] D. Wu, L. D. Zhao, S. Q. Hao, Q. K. Jiang, F. S. Zheng, J. W. Doak, H. J. Wu, H. Chi, Y. Gelbstein, C. Uher, C. Wolverton, M. Kanatzidis, J. Q. He, *J. Am. Chem. Soc.* **2014**, *136*, 11412.
[30] J. Goldak, C. S. Barrett, D. Innes, W. Youdelis, *J. Chem. Phys.* **1966**, *44*, 3323.
[31] H. Sun, X. Lu, H. Chi, D. T. Morelli, C. Uher, *Phys. Chem. Chem. Phys.* **2014**, *16*, 15570.
[32] R. H. Liu, L. L. Xi, H. L. Liu, X. Shi, W. Q. Zhang, L. D. Chen, *Chem. Commun.* **2012**, *48*, 3818.
[33] B. Wang, H. Xiang, T. Nakayama, J. Zhou, B. Li, *Phys. Rev. B* **2017**, *95*, 035201.
[34] D. P. Rai, Sandeep, A. Shankar, A. P. Sakhya, T. P. Sinha, P. Grima-Gallardo, H. Cabrera, R. Khenata, M. P. Ghimire, R. K. Thapa, *J. Alloys Compd.* **2017**, *699*, 1003.
[35] Z. Zhang, J. T. Yates, *Chem. Rev.* **2012**, *112*, 5520.

